JOURNAL OF MATERIALS SCIENCE 35 (2000) 6015–6026

Polymorphic transformation and powder characteristics of TiO_2 during high energy milling

RUIMING REN*, ZHENGUO YANG, L. L. SHAW
Department of Metallurgy and Materials Engineering, University of Connecticut, Storrs, CT 06269, USA
E-mail: lshaw@mail.ims.ucom.edu

Many studies have indicated that the reactivity of reactants can be enhanced greatly by mechanical activation through high energy ball milling. To understand this enhanced reactivity, the polymorphic transformation and the evolution of the powder characteristics of TiO_2 and graphite mixtures during high energy ball milling was investigated using various analytical instruments. It was found that polymorphic transformation of anatase to srilankite and rutile took place during milling. Furthermore, amorphization of crystalline phases and crystallization of the amorphous phase occurred at the same time during milling. High energy milling also led to ultrafine crystallites, large specific surface areas, and substantial amounts of defects in the powder particles. Effects of the graphite addition and the milling temperature on the polymorphic transformation and the evolution of the powder characteristics were also investigated. It was proposed that the polymorphic transformation of TiO_2 during milling could be explained in terms of the temperature-pressure phase diagram if the temperature rise and high pressure at the collision site were taken into consideration.

1. Introduction

The key enabling factor for widespread applications of nanostructured materials is the development of cost-effective, large-scale processes for synthesizing nanostructured materials [1]. Recently, we have reported a process that allows for large-scale production of nanostructured carbide powders from their oxides [2, 3]. The process combines mechanical and thermal activation to enhance the reaction of carbide formation. The basic form of the process is to high energy mill reactants at ambient temperature, which is followed by heating the milled reactants to high temperatures to complete the synthetic reaction. For example, to synthesize nanostructured TiC powder, TiO_2 and graphite are used as the starting materials, mixed and high energy ball milled at ambient temperature, and finally heated to high temperatures to complete the reaction of carbide formation. The product from this process is nanostructured TiC powder. Furthermore, in comparison with the current industrial carbothermic reduction [4], the new process has reduced the reaction temperature by about 500°C and the reaction time from 10–20 hours to 1–2 hours [2, 3]. Thus, the new process exhibits less energy consumption, higher production rates and better powder characteristics in comparison with the current industrial carbothermic reduction [2].

Mechanical activation has been studied extensively in synthesizing nanostructured crystalline materials *in-situ* during milling [5–21]. For this purpose the reactants with a negative free energy of formation at ambient temperature are typically used. For example, to synthesize nanostructured crystalline TiC through high energy milling, elemental Ti and C are used as the starting materials because the reaction between Ti and C has a negative free energy of formation. The negative free energy of formation provides the driving force for the formation of crystalline TiC compound *in-situ* during milling [13].

The concept of using high energy milling as an intermediate step to enhance the product formation has also been reported by several other research groups [22–31]. For example, it has been shown that the formation temperature of Fe-TiC composites based on carbothermic reduction of mineral ilmenite ($FeTiO_3$) can be substantially reduced by high energy milling before the reduction reaction [26]. The enhanced reduction reaction has been attributed to the intimate mixing and large contact area between milled ilmenite and carbon particles [27]. Short duration milling combined with low temperature annealing has also been successfully applied to the synthesis of $FeSi_2$, $MoSi_2$ and WSi_2 starting from elemental powders [23, 24, 29]. It has been shown that the temperature of disilicide formation from elemental powders can be reduced by as many as 400°C by high energy milling before the reaction [24]. The nitridation process can also be enhanced with mechanical activation, as demonstrated by the authors [30, 31] who have shown that the nitridation process of Si with N_2

* Visiting Scientist from Department of Materials Science and Engineering, Dalian Railway Institute, Dalian (116028), People's Republic of China.

can be accelerated by 9–23 times in comparison with the nitridation process of Si without mechanical activation. Recently, mechanical activation has also been used as an intermediate step before self-propagating high-temperature synthesis (SHS) [32, 33]. It is demonstrated that mechanical activation allows an ignition temperature decrease and an increase of the combustion front velocity over the classical SHS process.

In addition to being used to enhance the formation of compounds, mechanical activation has also been applied to enhancing the sintering process [34]. Working with a W-based alloy, Chausse *et al*. [34] have demonstrated that at the same sintering conditions, the mechanically treated powder exhibits a higher densification in comparison with the un-treated powder. The improved densification has been attributed to a faster diffusion rate and better mixing of W powder with the additive phase.

In brief, the previous examples have shown that many processes can be enhanced by mechanical treatment such as high energy milling. Obviously, an understanding of the mechanism responsible for the enhancement by high energy milling is necessary if mechanical activation will be utilized as an intermediate step for large scale production of nanostructured materials. As the first step towards this fundamental understanding, this study is aimed at the detailed investigation on the evolution of the phase content and microstructure of TiO_2 and graphite mixtures induced by high energy milling. The effect of these changes in the phase content and microstructure of the reactants on the formation of nanostructured TiC materials will be presented elsewhere.

2. Experimental

The starting materials of anatase-TiO_2 and graphite powders are shown in Fig. 1a. The anatase-TiO_2 of purity 99.95% had a spherical shape with about 0.2 μm in diameter, while the graphite of purity 99.9% exhibited a flake geometry with a thickness less than 0.2 μm and the other two dimensions up to about 10 μm. Powders with three different compositions, i.e., pure TiO_2, TiO_2 and graphite mixtures with carbon-to-titanium dioxide molar ratios of 3 : 1 and 4 : 1, were investigated. Unless otherwise mentioned, most of the results presented in this paper referred to TiO_2 and graphite mixtures with a molar ratio of 3 : 1. High energy milling was conducted using a modified Szegvari attritor that has been shown to be effective in producing uniform milling products within the powder charge [20]. Tungsten carbide (WC)

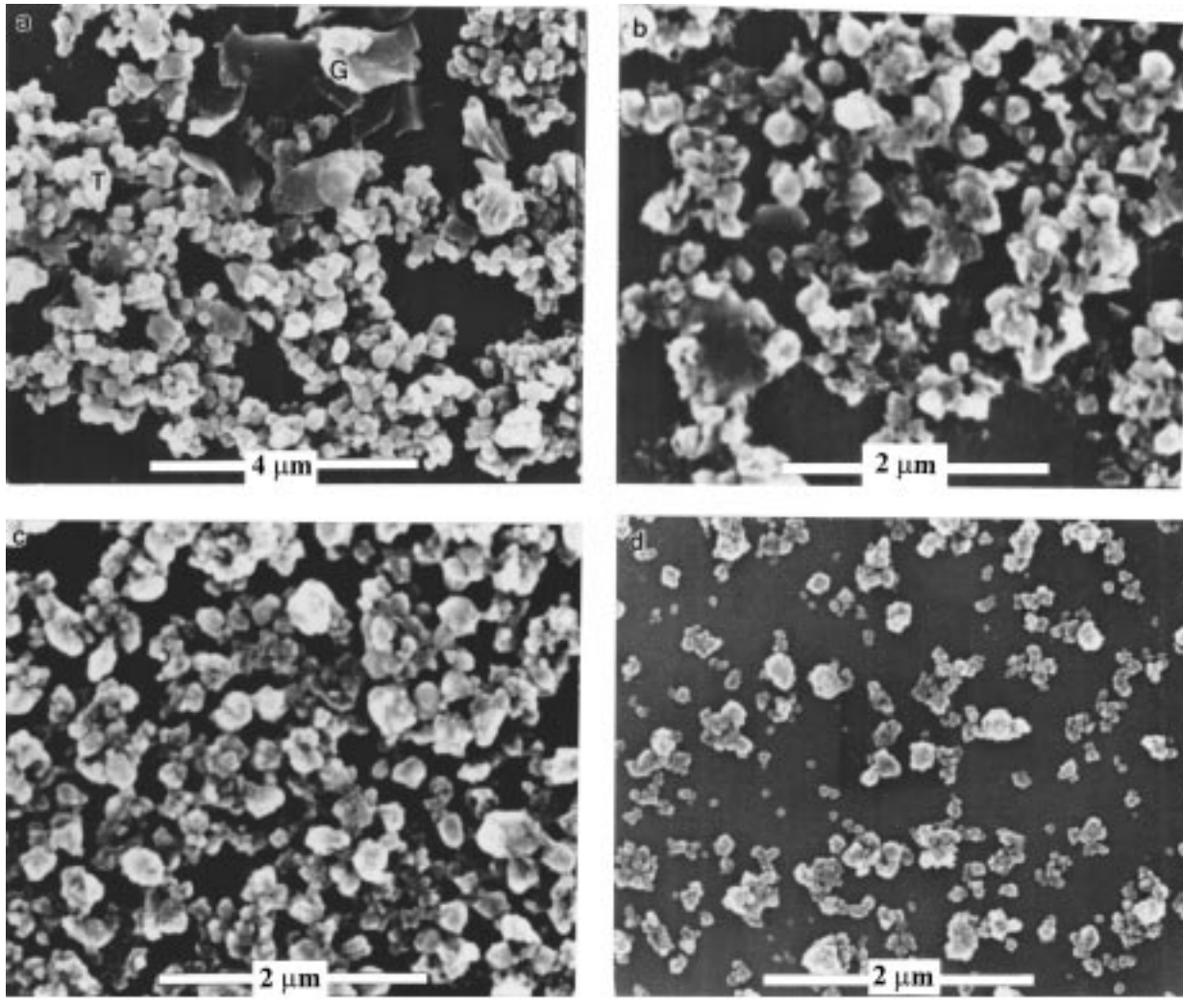

Figure 1 Environmental SEM images of TiO_2 and graphite powder mixtures: (a) before milling, (b) milled for 1.5 hours, (c) milled for 6 hours, and (d) milled for 24 hours. G and T in (a) refer to graphite and titanium dioxide, respectively.

balls (4.76 mm in diameter) were used as the milling media and mixed with powders at a ball-to-powder weight ratio of 60 : 1 for all the tests conducted. The charged canister was evacuated up to 10^{-2}–10^{-3} torr, flushed with argon, followed by evacuation and finally back filled with argon of purity 99.95% at a pressure of about 1.5 atm before the onset of milling. The canister was either cooled with circulation water at a flow rate of about 770 ml/min throughout the process (referred to as water cooling herein) or simply in contact with air (termed as air cooling hereafter). However, unless otherwise mentioned, most of the data presented were obtained using the water cooled condition. The temperature of the canister was monitored using an E-type thermocouple attached to the bottom of the canister. A milling speed of 600 RPM was employed for all the tests.

Phase identification of the milled powder mixtures was carried out using x-ray diffraction (XRD) methods with Cu K_α radiation. The average size of crystallites was determined based on XRD peak broadening (e.g., the (101) reflection was used for anatase) using the Scherrer formula [35]:

$$B_p(2\theta) = \frac{0.9\lambda}{D\cos\theta} \quad (1)$$

In Equation 1 D is the average dimensions of crystallites, $B_p(2\theta)$ is the broadening of the diffraction line measured at half maximum intensity, λ is the wave length of the x-ray radiation and θ is the Bragg angle. The correction for instrumental broadening was taken into account in the measurement of the peak broadening. This was done by comparing the breadth at half maximum intensity of the x-ray reflections between the high-temperature-annealed powder standard and the milled samples [36]

$$B_p^2(2\theta) = B_h^2(2\theta) - B_f^2(2\theta) \quad (2)$$

where $B_p(2\theta)$ is the half-maximum breadth if there were no instrumental broadening, and $B_h(2\theta)$ and $B_f(2\theta)$ are the breadth from the milled samples and the standard, respectively. No consideration of internal strains was included in the estimation of crystallite sizes because two well-defined x-ray diffraction peaks are normally needed in order to separate the effects of crystallite sizes and internal strains [37]. This was hard to achieve especially when milling time was long (see Fig. 2). However, the error introduced by neglecting the effect of internal strains was reasonably small because the crystallite size determined using Equation 1 was comparable to that determined using transmission electron microscopy (TEM), as will be shown in the Result section.

The relative amount of anatase, srilankite and rutile as a function of the milling time was obtained through the internal standard method of x-ray diffraction using crystalline α-Al_2O_3 as the additive [38]. In determining the relative amount of each phase the integrated areas of the (101), (110), (111) and (104) reflections were used for anatase, rutile, srilankite and α-Al_2O_3 respectively to avoid the peak overlap and all the integrated intensities were obtained using the PeakFit software to fit the XRD peaks with a confidence level of 97%.

Particle morphology observation and crystal structure determination were performed on a Philips EM420 analytical transmission electron microscope coupled with selected area electron diffraction (SAED) and micro-diffraction. The morphology and size of the milled powder were also characterized using an environmental scanning electron microscope (Phillips ESEM 2020). Specific surface area (SSA) analysis was carried out using nitrogen adsorption based on the Braunauer-Emmett-Teller (BET) theory [39] (Quantachrome NOVA 1000).

3. Experimental results

3.1. Evolution of x-ray diffraction patterns

XRD patterns of TiO_2 and graphite mixtures with a C-to-TiO_2 molar ratio of 3 : 1 as a function of the milling time are shown in Fig. 2. It can be seen that the starting TiO_2 powder comprises primarily anatase polymorph

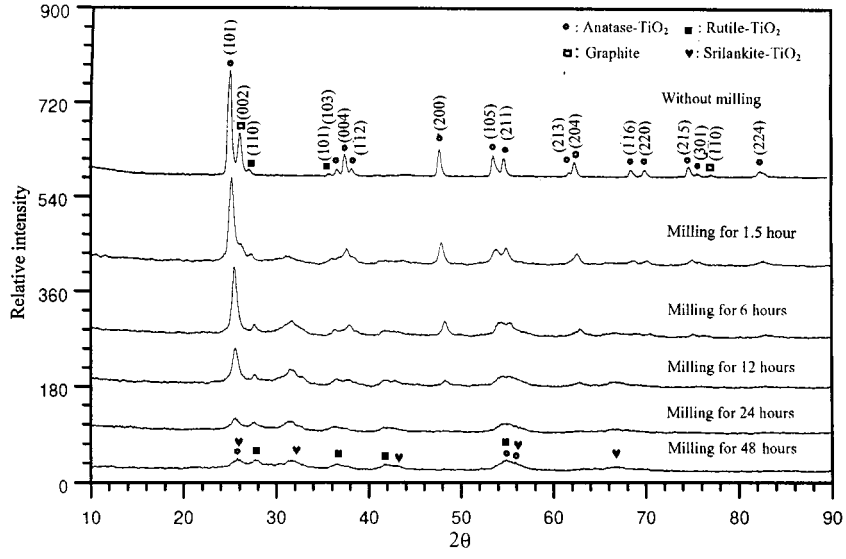

Figure 2 XRD patterns of TiO_2 and graphite mixtures as a function of the milling time.

with a small amount of rutile. Closer examination of Fig. 2 reveals several interesting features:

(1) The integrated area of graphite reflections decreases with increasing milling time and all the reflections disappear at 6-hours of milling. This may be due to the amorphization of graphite [13, 20, 40] and/or originate from the fact that the absorption of x-ray by titanium is much stronger than carbon, leading to extremely weak diffraction peaks of graphite relative to those of TiO_2 [41, 42]. Using TEM observation, however, we have confirmed that the peak disappearance of graphite is associated with the formation of an amorphous phase (see Figs 5 and 6).

(2) The integrated area of the anatase-TiO_2 reflections decreases with increasing milling time. As will be discussed later, the decrease of the integrated area of the anatase-TiO_2 reflections is partially caused by the transformation of some crystalline TiO_2 to the amorphous phase and partially due to the transformation of anatase to other TiO_2 crystalline structures.

(3) Reflections of srilankite-TiO_2 appear shortly after the onset of milling. Furthermore, the integrated area of srilankite-TiO_2 reflections increases at the early stage of milling, maximizes at about 6–12 hours of milling, and decreases afterwards.

(4) The integrated area of the rutile-TiO_2 reflections increases slightly with the milling time.

(5) Many reflections of anatase-TiO_2 such as the (116), (220), (215), (301) and (224) reflections disappear after milling for 12 hours, while many reflections of srilankite and rutile never appear. This suggests the extremely small correlation length of ordered stacking in the directions where the reflections disappear and/or the introduction of substantial amounts of defects in the crystalline TiO_2 phases.

(6) The preserved reflections of the remaining crystalline TiO_2 exhibit broadening, suggesting small sizes of crystallites and/or the presence of the internal strain.

3.2. Powder characteristics

Based on peak broadening (Fig. 2), the calculated crystallite size of anatase is found to be of the order of nanometers after milling for just 1.5 hours and continues to decrease with increasing milling time (Fig. 3). Because of the small Bragg peaks of rutile and srilankite, the size of their crystallites is hard to calculate accurately. An estimation based on peak broadening indicates that the crystallite size of rutile is in the range of 4.5–20.0 nm with a decrease in the size as the milling time increases. For srilankite, however, the size of its crystallites is estimated to be about 6 nm, nearly independent of the milling time.

The SEM examination of powder mixtures (Fig. 1) indicates that graphite flakes break down to particles at about 1.5-hour milling. Afterwards, the size of powder particles decreases slowly and reaches a lower limit of ∼100–400 nm at about 24-hours of milling. It is noted that the size of powder particles after 6-hours of milling is already of the order of submicrometers (∼400 nm). Thus, combined with the XRD data, it is believed that the milled submicrometer-sized powder particles are either crystalline with internal nanostructures of ∼6–20 nm and/or amorphous (see TEM below). Many other milled materials have also been found to possess such characteristics, that is, powder particles contain internal nanostructures, while the size of particles themselves is of the order of submicrometers or micrometers [12, 43–45].

The specific surface area of TiO_2-plus-graphite powder mixtures as a function of the milling time is shown in Fig. 4. It can be seen that the SSA of the powder mixtures increases sharply at the early stage of milling, peaks at about 6-hours of milling, and then decreases gradually. A similar phenomenon has also been observed in the SiO_2-plus-graphite powder mixtures that also exhibit their peak SSA at about 6-hours of milling [46].

A typical bright-field TEM image of TiO_2-plus-graphite powder mixtures milled for 6 hours is shown in Fig. 5. It is clearly shown that each particle observed in SEM (∼400 nm in diameter) is in fact composed of several large solid particles and many small particles. The analysis of TEM micro-diffraction indicates that the large solid particles (marked as A in the figure) are mainly anatase-TiO_2, while the small particles (that surround the large particles and are marked as G) are a mixture of nanocrystalline and amorphous phases, as indicated by the presence of both the diffuse amorphous

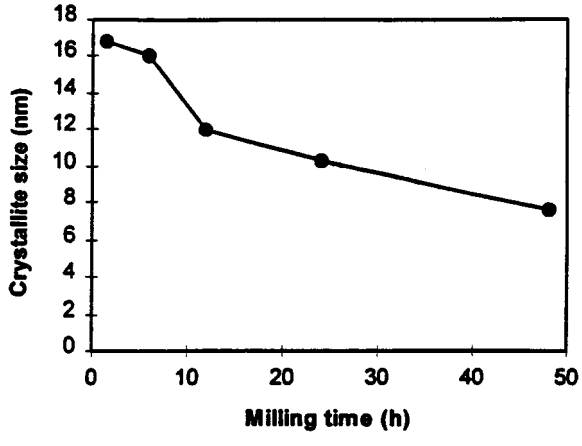

Figure 3 The crystallite size of anatase in TiO_2 and graphite mixtures as a function of the milling time, determined using the anatase (101) peak.

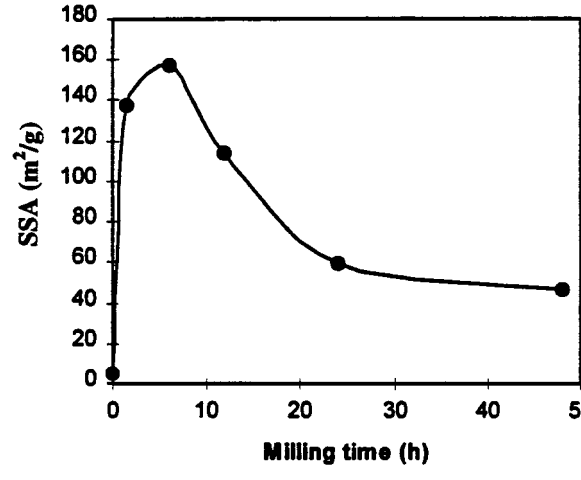

Figure 4 The specific surface area (SSA) of TiO_2 and graphite mixtures as a function of the milling time.

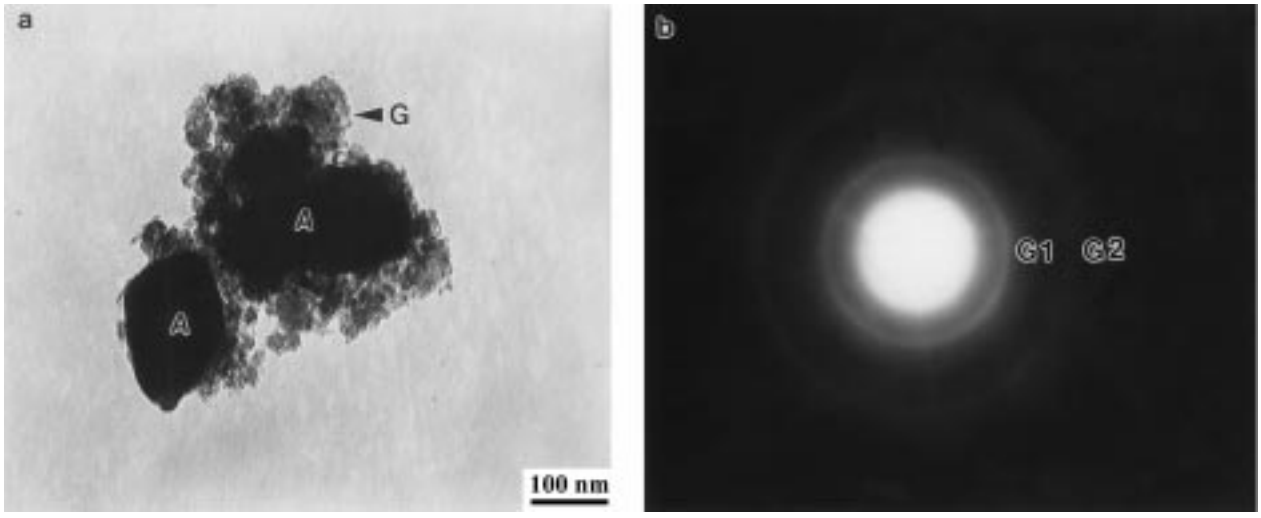

Figure 5 (a) A typical bright-field TEM image of TiO_2 and graphite mixtures milled for 6 hours, and (b) the corresponding micro-diffraction pattern of the small particles, G, in (a), taken with a camera length of 660 mm. The diffuse ring marked as G1 is located at the loci of the crystalline graphite (100) and (101) reflections, and the diffuse ring marked as G2 is where the loci of the crystalline graphite (110) and (112) reflections are.

ring and several broadened polycrystalline rings from these small particles (Fig. 5b). Furthermore, the positions of the broadened polycrystalline rings coincide with the positions of graphite reflections, suggesting that the small particles are primarily composed of carbon. Thus, graphite in the powder mixture is partially amorphized and the remaining crystalline graphite has extremely fine crystallites after 6-hours of milling.

A typical bright-field TEM image of TiO_2-plus-graphite powder mixtures milled for 24 hours is shown in Fig. 6. The image is similar to that of the powder mixture milled for 6 hours, i.e., each particle observed in SEM (∼400 nm in diameter) is composed of several large solid particles and many small particles. Furthermore, the large particles in Fig. 6 are again TiO_2, as in the case of 6-hours of milling. The small particles that surround the larger particles are still primarily composed of carbon, but with more amorphous and less crystalline constituents than those at 6-hours of milling, as indicated by the highly diffuse rings of the micro-diffraction pattern from those small particles (Fig. 6b).

Bright-field and dark-field TEM images of a large particle from powders milled for 48 hours and its corresponding selected area diffraction pattern (SADP) are shown in Fig. 7. Note that the size of the particle is ∼400 nm under SEM (not shown in Fig. 1). Thus, as in the case of 6-hours and 24-hours of milling, the large particle observed in SEM is again composed of several large particles and many small particles (see Fig. 7a). The diffuse ring at the locus of the anatase (101) reflection clearly indicates the presence of amorphous TiO_2. The diffraction spots that overlap with the diffuse ring confirm the presence of crystalline phases. The dark-field image (Fig. 7c) from the diffuse intensity of the hole-like ring of graphite (marked as G in Fig. 7b) shows that amorphous carbon is uniformly distributed within and/or on the surface of these particles. However, the dark-field image (Fig. 7d) from the anatase diffuse intensity at the (101) locus shows that small particles and the outer region of the large particles (the light gray area in the figure) are amorphous, whereas the inner region of the large particles (the dark gray area in the figure)

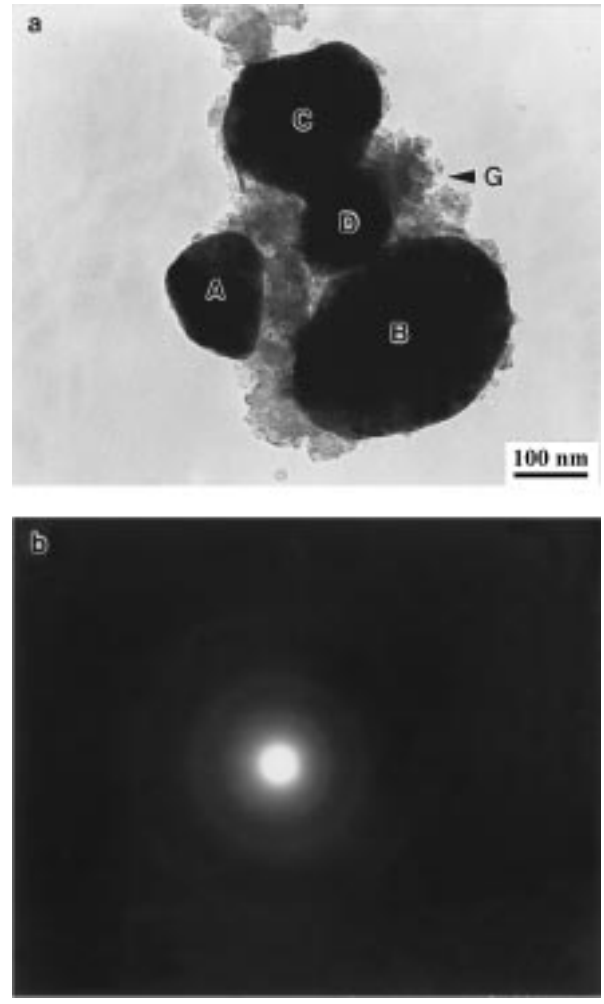

Figure 6 (a) A typical bright-field TEM image of TiO_2 and graphite mixtures milled for 24 hours, and (b) the corresponding micro-diffraction pattern of the small particles, G, in (a), taken with a camera length of 660 mm. A–D in (a) particles have been identified as TiO_2 using the micro-diffraction technique. Further, note that the diffraction rings from the small particles are much more diffuse than those shown in Fig. 5b.

still contains some degree of crystallinity; otherwise, the inner region should be light gray as well. Furthermore, the phase that contributes to the crystalline image must be primarily TiO_2 since Fig. 7c has indicated that

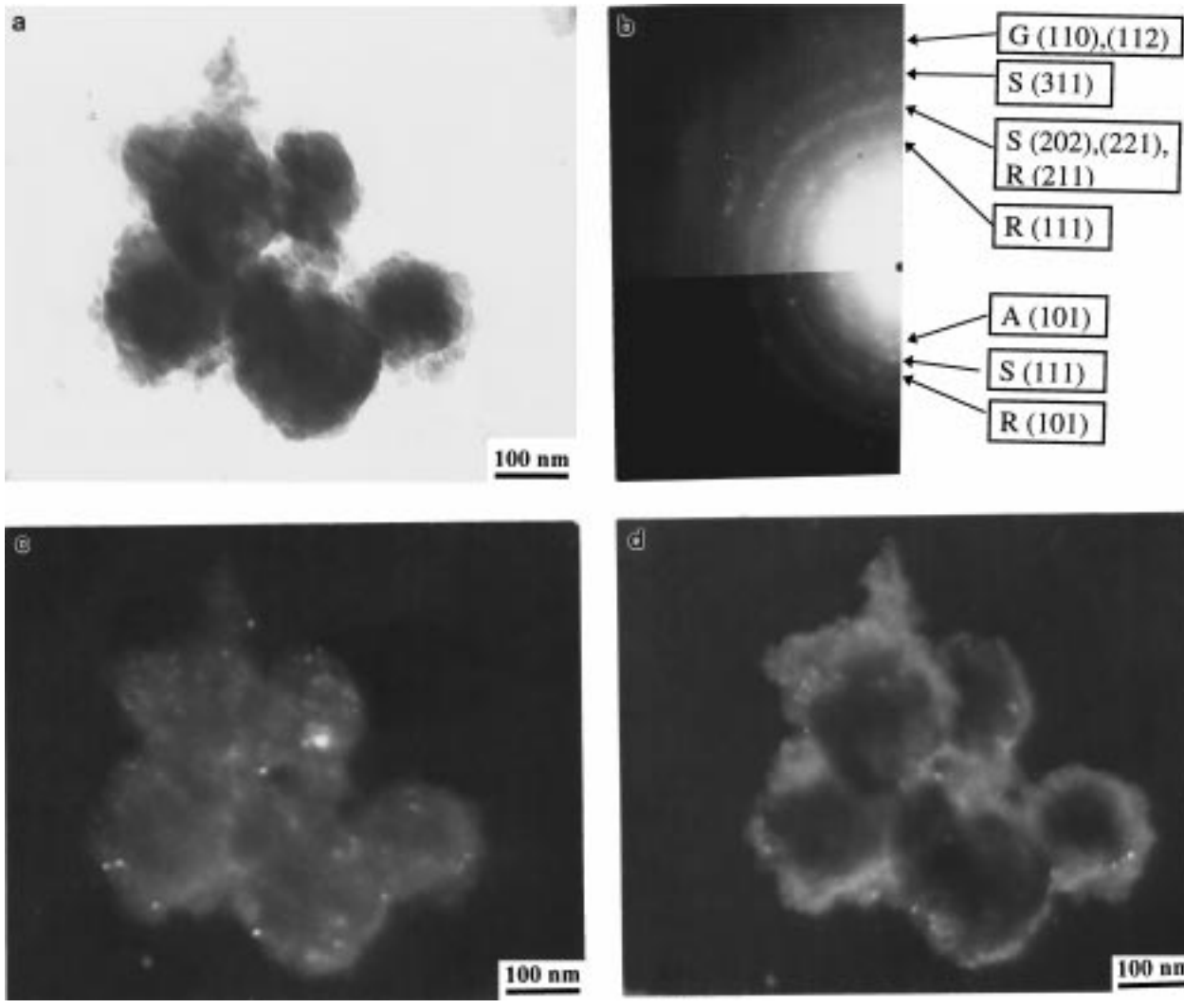

Figure 7 (a) A typical bright-field TEM image of TiO_2 and graphite mixtures milled for 48 hours, (b) the corresponding SAED patterns of the particles in (a), taken with a camera length of 950 mm, (c) the dark-field image of the particles in (a) from the diffuse intensity marked as the G (110) and (112) in (b), and (d) the dark-field image of the particles in (a) from the diffuse intensity marked as the A (101) in (b). G, S, R and A in (b) stand for graphite, srilankite, rutile and anatase, respectively, and the indexes associated with them indicate the loci of the specific reflections if the particles were 100% crystalline.

nearly all graphite has become amorphous at this stage of milling. Thus, these results indicate that at 48-hours of milling the small particles that surround the larger particles are composed of amorphous carbon and TiO_2. Moreover, the large particles observed with TEM are still predominately TiO_2, but with a large portion of amorphous constituents. These results also confirm that the integrated area decrease of anatase-TiO_2 reflections in XRD with milling is partially due to the transformation of some crystalline TiO_2 to the amorphous phase.

3.3. Effects of graphite addition

A comparison of XRD patterns among pure TiO_2 powder, TiO_2 and graphite powder mixtures with C-to-TiO_2 molar ratios of 3 : 1 and 4 : 1 milled for 1.5 hours is shown in Fig. 8. It is obvious from Fig. 8 that the integrated area of anatase reflections (e.g., the (101) reflection) for the pure TiO_2 powder sample is much smaller than that of anatase reflections for the TiO_2 and graphite mixtures. These results show that a large amount of anatase in the pure TiO_2 sample has been transformed to an amorphous state, whereas a large portion of anatase still remains in the TiO_2 and graphite mixtures. It is also noted that the XRD pattern of pure TiO_2 powder milled for 1.5 hours is very similar to that of the TiO_2 and graphite mixture with a molar ratio of 3 : 1 milled for 6 hours (Fig. 2). Thus, these results strongly suggest

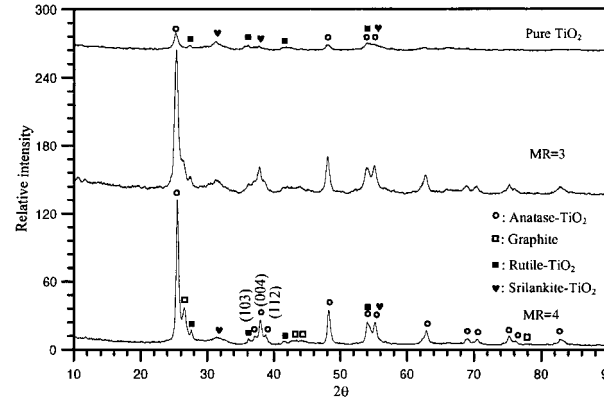

Figure 8 XRD patterns of pure TiO_2 powders and TiO_2 and graphite powder mixtures milled for 1.5 hours, showing the effects of graphite addition. MR represents the molar ratio of graphite to TiO_2.

that the addition of graphite reduces the rate with which anatase transforms to the amorphous phase and other crystalline phases.

Closer examination of the two TiO_2 and graphite powder mixtures also provides evidence in the reduction of the milling efficiency of reducing crystallite sizes, decreasing correlation lengths of ordered stacking, and introducing internal strains due to the presence of graphite. Fig. 8 shows that the XRD pattern of the powder mixture with a C-to-TiO_2 molar ratio of 4 : 1 has sharper reflections of anatase such as (103) and (112) peaks than those of the powder mixture with a C-to-TiO_2 molar ratio of 3 : 1. Diffuse reflections are an indication of extremely small crystallites, large internal strains and/or local correlated disorder. In fact, the estimation of the crystallite size of anatase based on peak broadening gives 14.2, 16.8 and 65.5 nm for pure TiO_2, the powder mixture with the 3 : 1 molar ratio and the powder mixture with the 4 : 1 molar ratio, respectively. Thus, the process of crystallite refinement has been slowed down by the presence of graphite. Similar phenomena have also been observed when graphite is added to SiO_2 [46], Si [30], Ti and Nb [47].

3.4. Effects of cooling media

It was found that the average environmental milling temperature for the water cooling condition was constant at about 20°C throughout the milling process, while it increased gradually at the beginning of milling and stabilized at about 120°C after milling for 0.5 hours for air cooling. Thus, the average temperature difference between water cooling and air cooling is about 100°C after 0.5-hours of milling. XRD patterns of TiO_2 and graphite powder mixtures milled with water cooling and air cooling for 24 hours are shown in Fig. 9. Effects of cooling media can be examined by comparing the ratios of the integrated area of anatase (101) reflection to the integrated area of srilankite (111) reflection and to the integrated area of rutile (110) reflection for water cooling with those for air cooling. The result is summarized in Table I. It is clear from the table that there is less crystalline anatase and/or more srilankite and rutile in the air cooled specimen than in the water cooled specimen, suggesting that milling under air cooling conditions leads to the transformation of more anatase to amorphous phase and/or srilankite and rutile.

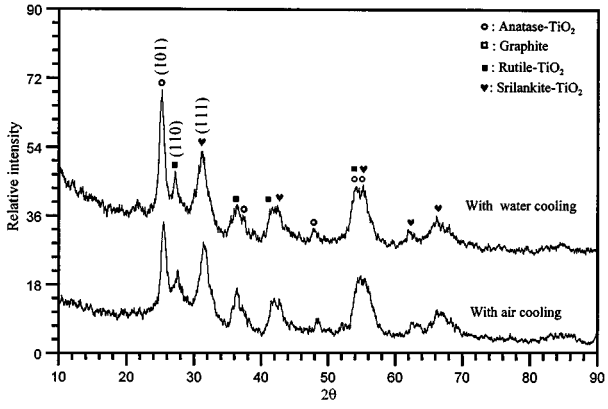

Figure 9 XRD patterns of TiO_2 and graphite powder mixtures milled for 24 hours, showing the effects of cooling media.

TABLE I Ratios of the integrated area of anatase (101) reflection to the integrated area of srilankite (111) reflection, $R_{A/S}$, and to the integrated area of rutile (110) reflection, $R_{A/R}$

Milling Conditions	$R_{A/S}$	$R_{A/R}$
24-hour milling, C-to-TiO_2 ratio = 4 : 1, and water cooling	0.79	1.82
24-hour milling, C-to-TiO_2 ratio = 4 : 1, and air cooling	0.64	1.11

4. Discussion

4.1. Polymorphic transformations of TiO_2

Extensive work [48–51] has indicated that there exist five polymorphs of TiO_2: anatase, brookite, srilankite, TiO_2-III and rutile. Anatase and brookite are low-temperature, low-pressure forms; srilankite and TiO_2-III are formed from anatase or brookite under pressure; and anatase transforms to rutile very slowly at 610°C under ambient pressure [50]. A temperature-pressure phase diagram showing relationship among anatase, rutile and srilankite from Murray and Wriedt [52] is shown in Fig. 10. Many phenomena observed in this study can be explained based on this phase diagram. According to Fig. 10, anatase can transform to srilankite at high pressures and to rutile at high temperatures. Anatase can also transform to an amorphous phase, as observed in this study (Figs 2 and 7). The transformation of crystalline phases to amorphous phases during high energy milling is a well-known phenomenon. It has been established that for pure materials amorphization can be induced by high pressures and/or crystallite refinement [45], while for mixtures of several materials amorphization can also be induced by a solid-state interdiffusion reaction [53] and a gas-solid reaction [30]. One mechanism for the pressure-induced amorphization is that the compressive pressure during ball collision exceeds the metastable extension of the liquidus curve on the T-P phase diagram; thus, the amorphous phase is formed directly on compression and persists on separation of ball and powder [45]. Amorphization of crystalline compounds caused by high energy milling has been observed in many metal and ceramic systems such as SiO_2 [46], YCo_3 [54], $Ni_{45}Nb_{55}$ [54], $NiZr_2$

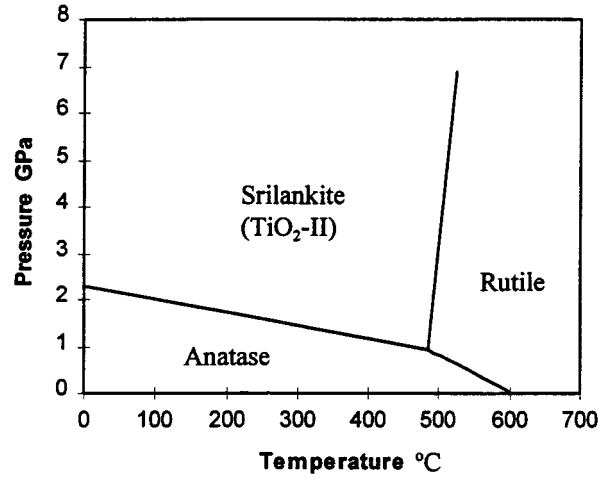

Figure 10 A nonequilibrium temperature-pressure phase diagram of pure TiO_2 [52].

[55, 56], Nb_3Sn [56] and Ni_3Al [56]. In all these cases the free energy of the amorphous phase is higher than that of the corresponding crystalline phase. The excess free energy required for amorphization comes from the introduction of structural defects and refinement of crystallites in the crystalline phase during milling [53]. For the present system, it is believed that the driving force for the amorphization of anatase also comes from the crystallite refinement and the introduction of considerable defects. Furthermore, the evidence collected also indicates that during milling the transformation of anatase to srilankite, to rutile and to an amorphous phase takes place at the same time. This is discussed below in more detail.

As seen in Fig. 2, the formation of srilankite occurs shortly after the onset of milling (less than 1.5 hours), suggesting that srilankite is formed directly from crystalline anatase since there is hardly any amorphous phase at the early stage of milling. According to Fig. 10, this result also implies that the pressure experienced by anatase powder particles during collision of two colliding balls is likely to be above 1 GPa. The increase in the defect density of anatase due to milling may reduce the lower pressure limit required for the transformation of anatase to srilankite. In that case, a collision pressure lower than 1 GPa may be enough to induce the anatase-to-srilankite transformation. Nevertheless, by utilizing the approach of the Hertz impact theory and fluid mechanics to approximate the ball milling process as proposed by Maurice and Courtney [57], we have estimated the maximum pressure reached on collision for the milling conditions employed in this study and found it to be 6 GPa (see the Appendix). The presence of powder during collision will certainly reduce the pressure reached on collision. Nevertheless, the pressure experienced by some particles is expected to be still higher than 1 GPa (see the Appendix). Thus, the pressure experienced by some particles is high enough to trigger the anatase-to-srilankite transformation on compression of two colliding balls. Thus, it can be concluded that srilankite is formed directly from anatase on collision under the present milling condition.

To quantify the relative amount of anatase, srilankite and rutile as a function of the milling time, the internal standard method of x-ray diffraction using Al_2O_3 as the additive was conducted. The result is shown in Fig. 11. It can be seen that the amount of srilankite peaks at about 6–12 hours. This suggests that while srilankite is formed from anatase, srilankite also transforms to other phases such as the amorphous phase and/or rutile; otherwise, the amount of srilankite should not decrease with further milling.

Fig. 11 also exhibits that the amount of rutile continues to increase with milling. However, the rate with which rutile increases is small in the whole milling range studied (from 0 to 48 hours). The formation of rutile is likely from several different sources or at least two sources: anatase and the amorphous phase. At the early stage of milling, rutile is likely formed from anatase since the amount of other phases such as srilankite and the amorphous phase is literally zero. The small increase rate of rutile in comparison with the increase rate of srilankite at the early stage of milling is likely related

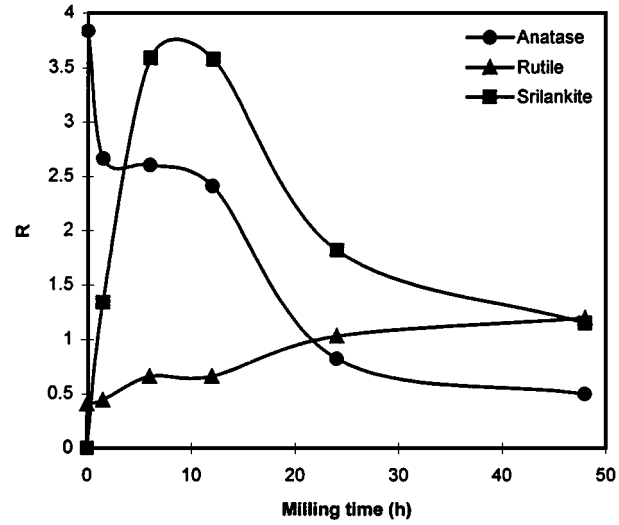

Figure 11 The relative amount of anatase, srilankite and rutile as a function of the milling time. *R* is the ratio of the integrated areas of particular XRD reflections according to the following formulae: $I_{(101)TiO2}/I_{(104)Al2O3}$ for anatase, $I_{(110)TiO2}/I_{(104)Al2O3}$ for rutile and $I_{(111)TiO2}/I_{(104)Al2O3}$ for srilankite.

to the high temperatures required for the transformation of anatase to rutile. According to Fig. 10, rutile can be formed from anatase as long as a minimum temperature higher than 480°C is reached. Many studies have suggested the local temperature of powder particles at the collision site can have 180°C [58], 350°C [59] and 500°C [54] higher than the average environmental temperature, depending on the milling conditions and powder characteristics. Using the formula proposed by Schwarz and Koch [54], the temperature increase of the anatase powder caused by the impact of the milling media for the present milling conditions is estimated to be 325°C (see the Appendix). Thus, the local temperature at the collision site could reach about 350°C for water cooling and about 450°C for air cooling in this study. These temperatures are lower than the minimum requirement (480°C) for the formation of rutile from anatase and srilankite. However, the increased defect density in anatase due to milling could reduce the minimum transformation temperature to below 480°C. Nevertheless, the increase rate of rutile is not expected to be as large as that of srilankite because the high pressure requirement for forming srilankite is satisfied at the onset of milling, whereas the anatase-to-rutile transformation relies on the build-up of defects in anatase via milling.

At the later stage of milling the continued increase of rutile is likely associated with crystallization of the amorphous phase because the amount of anatase has decreased sharply after 12-hours of milling. Furthermore, the postulation that the continued increase of rutile at the later stage of milling is primarily due to crystallization of the amorphous phase is also supported by consideration of transformation temperatures. The crystallization temperature of the amorphous phase should be lower than the anatase-to-rutile transformation temperature because of the larger driving force of the amorphous phase to form rutile than that of anatase to form rutile. Thus, crystallization of the amorphous phase would be easier than the anatase-to-rutile transformation. Furthermore, rutile as the crystallization product

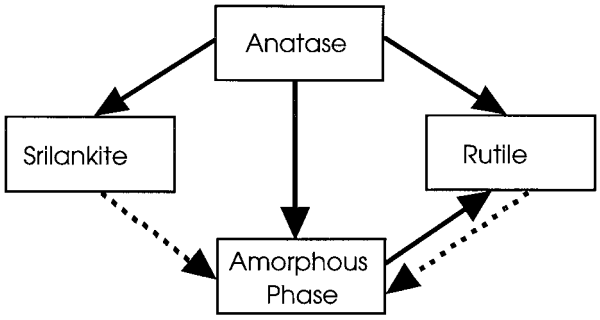

Figure 12 Various transformations related to milling of TiO_2. Solid arrow(s) indicate the most likely transformation, whereas the dashed arrow(s) stand for the possible or negligible transformation.

is consistent with the fact that rutile is the stable phase in comparison with anatase [48, 52, 60].

In short, the polymorphic transformation of TiO_2 during milling in this study can be summarized in Fig. 12. During milling, anatase transforms to srilankite, rutile and the amorphous phase: Srilankite and rutile may also transform to the amorphous phase, whereas the amorphous phase can crystallize to form rutile. Finally, it is interesting to point out that many researchers [55, 61] have also reported simultaneous amorphization and crystallization during milling of other metallic compounds.

Finally, it should be mentioned that polymorphic transformations of TiO_2 discussed above may also be affected by the contamination of the powder with materials from the wear of the milling tools, especially the wear of balls in the case of attritors. By measuring the weight loss of WC balls after several thousand hours of milling, the wear rate of WC balls is estimated to be 5.5 mg/hr under the present milling condition. Although the wear rate is small, it may have effects on polymorphic transformation of TiO_2. For example, the anatase-to-srilankite transformation occurs at less than 1.5-hours of milling and the weight percent of WC in the powder at this milling time is about 0.03 wt.%. Although small, such contamination may alter the temperature of the anatase-to-srilankite transformation slightly.

4.2. Evolution of powder characteristics

The present study indicates that in addition to the polymorphic transformation, high energy milling of TiO_2 and graphite mixtures also leads to the particle refinement, crystallite refinement, agglomeration of fine particles, and mixing of TiO_2 and carbon on nanometer scales. Under the present milling condition, it seems that the crystallite size of anatase-TiO_2 continues to decrease with increasing the milling time (Fig. 3). This is believed to result primarily from the fundamental process of repeated plastic deformation during milling. A recent study on high energy milling of Si [62] has established that the particle size of Si during milling is controlled by fragmentation, whereas the crystallite size is dictated by repeated plastic deformation. Although it looks that the crystallite refinement will continue as milling procceds beyond 48 hours in this study, it is expected that this will cease when recrystallization sets in or all the crystalline phase becomes amorphous.

The SEM examination (Fig. 1) has clearly shown that the average particle size of the TiO_2 and graphite mixture decreases gradually up to 24-hours of milling after which a lower limit of the particle size is reached. The little change of the average particle size of the powder mixture beyond 24-hours of milling is likely related to a dynamic balance among fragmentation, coalescence and agglomeration of nanoparticles.

A detailed comparison between the SEM observation (Fig. 1) and the SSA measurement (Fig. 4) seems to suggest a discrepancy between these two analyses; that is, the SEM observation suggests that the SSA of the powder mixture milled for 6 hours should be lower than that of the powder mixture milled for longer times, whereas the SSA measurement reveals that the SSA peaks at 6-hours of milling. It is noted that the trend of the SSA change with milling measured in this study is also observed in the SiO_2-plus-graphite powder mixture [46] and the pure graphite powder system measured by Hermann *et al*. [63]. Their results show a sharp increase in the SSA of graphite to $\sim$600 m^2/g at $\sim$3-hours of milling, which is followed by a gradual decrease to $\sim$200 m^2/g at 50-hours of milling. The decrease in the SSA beyond 3-hours of milling has been attributed to agglomeration of graphite nanoparticles [63]. However, it is well known that physical agglomeration cannot drastically decrease the SSA measured using the BET method. Thus, we believe that the change of the SSA of either pure graphite or graphite-containing powder mixtures with milling time must be dictated by other fundamental processes rather than agglomeration.

Our recent work on SiO_2-plus-graphite powder system [46] has indicated that the SSA change with milling time is related to the fact of easy delamination of graphite along its basal plane. It is shown that at the early stage of milling bulk graphite becomes flakes due to its easy delamination. As milling time increases to 6 hours, the graphite flakes become extremely fine and some of graphite has become amorphous. However, beyond 6-hours of milling the morphology of graphite changes from fine flakes to granular shapes due to the formation of the amorphous phase. As such, the SSA peaks at 6-hours of milling. Such mechanism is also likely to operate in the present TiO_2-plus-graphite system and in the pure graphite system mentioned above.

4.3. Effects of graphite addition

The reduced milling efficiency by the presence of graphite is likely related to the ease with which graphite delaminates along its basal plane, thereby providing a lubricating function and limiting the build-up of pressure on collision. Thus, the more graphite present, the slower the crystallite refinement process and the less transformation of anatase to srilankite and amorphous phase. In addition, there is no chemical reaction between graphite and TiO_2 during milling. This is believed to be due to no chemical driving forces for reactions, as shown in the following equation assuming the contact of TiO_2 with C at ambient temperature and under 1 atmosphere of CO_2.

$$TiO_2 + 2C = TiC + CO_2 \quad \Delta G_{298} = 302{,}700 \text{ J/mol} \tag{3}$$

TiC will only form at temperatures above 564°C if a 10^{-4} torr of CO_2 is assumed [64]. This temperature is above the local temperature on the collision site calculated previously. Thus, the function of graphite in this study is to provide lubrication and reduce the average pressure on collision.

4.4. Effects of milling temperature

Increasing the average environmental milling temperature leads to an increased local temperature at the collision site. Thus, the local temperature at the collision site for air cooling is higher than that for water cooling. The diffusivity of atoms increases and the pressure required for the transformation of anatase to srilankite and rutile decreases with increasing temperature (Fig. 10). The higher the diffusivity of atoms, the more transformation products form in a given collision time. Since the pressure required for forming srilankite and rutile from anatase lowers with increasing temperature, more powder particles will meet the transformation pressure requirement and therefore more srilankite and rutile are formed on each collision when the environmental temperature (and therefore the local temperature) is increased. Thus, the enhanced formation of rutile and srilankite by changing from water cooling to air cooling (Fig. 9 and Table I) is consistent with these arguments.

5. Concluding remarks

Systematic studies have been carried out to investigate the polymorphic transformation and the evolution of the powder characteristics of TiO_2 and graphite mixtures during high energy milling. Effects of the addition of graphite and the milling temperature on the milling efficiency have also been investigated. Based on these studies, the following conclusions can be offered:

(1) Polymorphic transformation of anatase-TiO_2 to rutile and srilankite polymorphs takes place during high energy ball milling.

(2) In addition to polymorphic transformation, amorphization of TiO_2 also occurs during high energy milling.

(3) Most of graphite in the powder mixture is amorphized after 6-hours of milling.

(4) The crystalline phases present during milling have ultrafine crystallites, possess substantial amounts of defects, and have large specific surface areas.

(5) The addition of graphite to TiO_2 powders slows down the milling process including both crystallite refinement and polymorphic transformation. This is due to the lubrication effect of graphite.

(6) The higher the average environmental milling temperature is, the faster the milling process is. This includes crystallite refinement and polymorphic transformation.

Appendix of calculations

1. The average pressure at maximum compression on collision

Maurice and Courtney [57] analyze the average pressure developed across the contacting surfaces of the milling media at maximum compression using the Hertz theory:

$$P_{\max} = 0.4646 v^{0.4} \left(\frac{\rho}{E}\right)^{0.2} E \tag{A1}$$

where E is the elastic modulus of the balls, ρ is the density of the balls, and v is the precollision relative velocity that is computed through

$$v = 1/3 \omega R_a \tag{A2}$$

with ω being the rotational velocity of the impeller arms and R_a the radius of the canister. For WC balls, a milling speed of 600 RPM and $R_a = 44$ mm, we have

$v = 0.146$ m/s, $\rho = 14.29$ g/cm^3, E = 600 GPa

and $P_{\max} = 6089$ MPa

2. The average pressure on collision with powder

The average pressure experienced by powder particles on collision is certainly lower than that computed with no powder between two colliding balls using Equation A1 because some of the kinetic energy will be consumed by friction among powder particles and fracture of particles. How high the average pressure of powder particles reaches on collision is primarily dependent of the kinetic energy of two colliding balls, mechanical properties of powder aggregates, and the loading conditions. The kinetic energy of two colliding balls is approximately equal to the elastic energy, U_E, of the two colliding balls when there are no powder particles between them and can be calculated as follows [57]:

$$U_E = \frac{P_{\max}^2}{2E} \frac{2\pi R^2 \delta_{\max}}{3} \tag{A3}$$

where R is the radius of the ball, $\delta_{\max}$ is the distance the center of masses of the two balls are displaced relative to each other during the collision, and $P_{\max}$ and E have been defined above. $\delta_{\max}$ can be computed using the Hertz theory [57]:

$$\delta_{\max} = 1.89 v^{0.8} \left(\frac{\rho}{E}\right)^{0.4} R \tag{A4}$$

With $R = 4.76$ mm, we have $\delta_{\max} = 0.0398$ mm and $U_E = 4.98$ J. Assuming that all this elastic energy has been consumed to deform and fracture the powder particles trapped between the two colliding balls, then

$$U_E = U_{\text{friction}} + U_F \tag{A5}$$

where U_{friction} and U_F stand for the energy consumed by friction among particles and fracture of particles, respectively. Generally, U_{friction} is small in comparison with U_F; thus, Equation (A5) can be approximated as

$$U_E \approx U_F \tag{A6}$$

Furthermore, the energy required to fracture the powder particles trapped between two colliding balls, U'_F, is [57]

$$U'_F = \pi r^2 h_0 u_f \tag{A7}$$

where u_f is the fracture energy per unit volume of powder particles, r is the radius of the Hertz impact, and h_0 is the initial height of the powder aggregate trapped between two colliding balls. The parameter, $\pi r^2 h_0$, in Equation A7 corresponds to the volume of powder particles trapped between the two colliding balls. r and h_0 can be found with the aid of [57]

$$r = 0.9371 v^{0.4} \left(\frac{\rho}{E}\right)^{0.2} R \tag{A8}$$

$$h_0 = 0.27 \frac{R\rho}{\rho_p C_R} \tag{A9}$$

where C_R is the ball-to-powder weight ratio (i.e., the charge ratio), and ρ_p is the density of the powder particles. With $C_R = 60$ (i.e., the charge ratio used in this study) and $\rho_p = 4.0$ g/cm^3 [65], we have $r = 0.097$ mm and $h_0 = 0.076$ mm.

The fracture energy per unit volume of powder particles can be calculated from properties of powder particles:

$$u_f = \frac{\sigma_f^2}{2E_p} \tag{A10}$$

where σ_f is the fracture strength in compression, and E_p is the elastic modulus of powder particles. Assuming the powder particles are composed of 100% TiO_2 and taking the uniaxial compressive strength of TiO_2 as 900 MPa and $E_p = 282$ GPa [65], the fracture energy per unit volume of TiO_2 particles is found to be 1.436×10^6 J/m^3.

Substituting the values of u_f, r and h_0 into Equation (A7), we obtain $U'_F = 3.27 \times 10^{-6}$ J/m^3. By comparing U'_F (the energy required to fracture the powder particles trapped) and U_F (the energy available for fracturing the powder particles trapped), we have that U_F is six orders of magnitude higher than U'_F. Thus, fragmentation of TiO_2 particles will take place constantly under the milling conditions used in this study. If a TiO_2 particle fractures under a uniaxial compression, the pressure experienced by that particle will certainly not exceed the compressive strength (900 MPa). However, statistically some particles certainly experience multiaxial compression due to constraints from neighboring particles on collision. It is well known that the strength of a brittle material (e.g., TiO_2) under multiaxial compressive loading could be much higher than the uniaxial compressive strength. Since the previous calculation has indicated that in addition to fracturing particles there is still a substantial amount of extra energy available for multiaxial compression, it is expected that some of the particles must have a compressive stress component exceeding 1 GPa on collision.

3. The temperature rise at the collision site

Schwarz and Koch [54] analyze the temperature rise resulting from localized shear of powder particles trapped between two colliding balls:

$$\Delta T = \frac{P_{max}\, v}{2} \left(\frac{\tau}{\pi k_0 \rho_p C_p}\right)^{1/2} \tag{A11}$$

where k_0 is thermal conductivity of the powder, ρ_p is the powder particle density, C_p is the specific heat of powder and Pmax, v and t have been defined above. For anatase-TiO_2 powder, typical values are [65]:

$$k_0 = 8.4 \text{ w/m.K}, \quad \rho_p = 3.84 \text{ g/cm}^3,$$
$$C_p = 800 \text{ J/kg·K}$$

On substitution of these values into Equation A11, $\Delta T = 325^\circ$C.

References

1. J. OUELLETTE, *Ind. Phys.* (June 1997) 15.
2. R.-M. REN, Z.-G. YANG and L. SHAW, *Scripta Mater.* **38**(5) (1998) 735.
3. *Idem., Ceram. Eng. Sci. Proc.* **19**(4) (1998) 461.
4. J. H. WESTBROOK and E. R. STOVER, in "High-Temperature Materials and Technology," edited by I. E. Campbell and E. M. Sherwood (John Wiley & Sons, Inc., 1967) p. 312.
5. H. J. FECHT, *Nanostructured Mater.* **1** (1992) 125.
6. R. NAGARAJAN, B. S. MURTY and S. RANGANATHAN, *Chin. J. Mater. Res.* **5** (Suppl.) (1994) 215.
7. F. H. FROES and J. J. DE BARBADILLO (eds.), "Structural Applications of Mechanical Alloying," (ASM International, Metals Park, OH, 1990).
8. R. B. SCHWARZ, S. R. SRINIVASAN, J. J. PETROVIC and C. J. MAGGIORE, *Mater. Sci. Eng.* **A155** (1992) 75.
9. S. JAYASHANKAR and M. J. KAUFMAN, *Scripta Metall. Mater.* **26** (1992) 1245.
10. C. C. KOCH, in "Nanophases and Nanocrystalline Structures," edited by R. D. Shull and J. M. Sanchez (The Minerals, Metals & Materials Society, Warrendale, PA, 1994) p. 19.
11. R. J. PEREZ, B. HUANG and E. J. LAVERNIA, *Nanostruct. Mater.* **7**(5) (1996) 565.
12. A. CALKA, A. P. RADLINSKI, R. A. SHANKS and A. P. POGANY, *J. Mater. Sci. Letter* **10** (1991) 734.
13. L. L. YE and M. X. QUAN, *Nanostruct. Mater.* **5** (1995) 2.
14. A. CALKA and J. S. WILLIAMS, *Scripta Metall. Mater.* **27** (1992) 999.
15. G. LE CAER, E. BAUER-GROSSE, A. PIANELLI, E. BOUZY and P. MATTEAZZI, *J. Mater. Sci.* **25** (1990) 4726.
16. P. MATTEAZZI and G. L. CAER, *J. Am. Ceram. Soc.* **74**(6) (1991) 1382.
17. M. SHERIF EL-ESKANDARANY, K. SUMIYAMA and K. SUZUKI, *J. Mater. Res.* **10** (1995) 659.
18. A. P. RADLINSKI and A. CALKA, *Mater. Sci. Eng.* **A134** (1991) 1376.
19. J. I. NIKOLOV, A. CALKA and J. S. WILLIAMS, *Nanostruct. Mater.* **6** (1995) 401.
20. Z.-G. YANG and L. SHAW, *ibid.* **7**(8) (1996) 873.
21. G. B. SCHAFFER and P. G. MCCORMICK, *Metall. Trans.* **22A** (1991) 3019.
22. N. J. WELHAM, *Minerals Eng.* **9**(12) (1996) 1189.
23. N. MALHOUROURX-GAFFET and E. GAFFET, *J. Alloys & Compounds* **198** (1993) 143.
24. E. GAFFET and N. MALHOUROURX-GAFFET, *ibid.* **205** (1994) 27.
25. Y. CHEN, *J. Mater. Sci. Letters* **16** (1997) 37.
26. *Idem., Scripta Mater.* **36**(9) (1997) 989.

27. Y. CHEN, T. HWANG, M. MARSH and J. S. WILLIAMS, *Metall. Mater. Trans.* **28A**(5) (1997) 1115.
28. E. GAFFET, M. ABDELLAOUI and N. MALHOUROURX-GAFFET, *Mater. Trans. JIM*, **36**(2) (1995) 198.
29. N. MALHOUROURX-GAFFET and E. GAFFET, *J. Alloys & Compounds* **198** (1993) 143.
30. L. SHAW, Z.-G. YANG and R.-M. REN, *Mater. Sci. Eng.* **A244** (1998) 113.
31. *Idem., J. Am. Ceram. Soc.* **81**(3) (1998) 760.
32. E. GAFFET, F. BERNARD, J.-C. NIEPCE, F. CHARLOT, C. GRAS, G. LE CAËR, J. L. GUICHARD, P. DELCROIX, A. MOCELLIN and O. TILLEMENT, *J. Materials Chemistry* **9** (1999) 305.
33. F. CHARLOT, F. BERNARD, E. GAFFET, D. KLEIN and J. C. NIEPCE, *Acta Mater.* **47**(2) (1999) 619.
34. C. CHAUSSE, F. NARDOU and E. GAFFET, in "Mechanically Alloyed and Nanocrystalline Materials," edited by A. R. Yavari (Mater. Sci. Forum, 1995) pp. 179 and 391.
35. H. P. KLUG and L. E. ALEXANDER, "X-Ray Diffraction Procedures for Polycrystalline and Amorphous Materials" (John Wiley & Sons, Inc., London, 1954) p. 491.
36. B. E. WARREN, "X-Ray Diffraction" (Dover Publications, Inc., New York, 1990).
37. W. H. HALL, *Proc. Phys. Soc. London* **A62** (1949) 741.
38. R. JENKINS and R. L. SNYDER, "Introduction to X-Ray Powder Diffraction" (John Wiley & Sons, Inc., New York, 1996).
39. S. BRAUNAUER, P. H. EMMETT and E. TELLER, *J. Am. Chem. Soc.* **60** (1938) 309.
40. A. CALKA and J. S. WILLIAMS, *Scripta Metall. Mater.* **27** (1992) 999.
41. B. C. CULLITY, "Elements of X-Ray Diffraction," 2nd ed. (Addison-Wesley, Reading, MA, 1978).
42. J. TANG, W. ZHAO, L. LI, A. U. FALSTER, W. B. SIMMONS, JR., W. L. ZHOU, Y. IKUHARA and J. H. ZHANG, *J. Mater. Res.* **11**(3) (1996) 733.
43. H. J. FECHT, E. HELLSTERN, Z. FU and W. L. JOHNSON, *Metall. Trans.* **21A** (1990) 2333.
44. E. WANG, G. LIANG and X. WANG, *Chin. J. Mater. Res.* **5**(Supp.) (1994) 202.
45. T. D. SHEN, C. C. KOCH, T. L. MCCORMICK, R. J. NEMANICH, J. Y. HUANG and J. G. HUANG, *J. Mater. Res.* **10** (1995) 139.
46. L. SHAW, R.-M. REN and Z.-G. YANG, unpublished research.
47. Z. G. LIU, L. L. YE, J. T. GUO, G. S. LI and Z. Q. HU, *J. Mater. Res.* **10**(12) (1995) 3129.
48. F. DACHILLE, P. Y. SIMONS and R. ROY, *Am. Min.* **53** (1968) 1929.
49. M. NICOL and M. Y. FONG, *J. Chem. Phys.* **54**(7) (1971) 3167.
50. A. W. CZANDERNA, C. N. R. RAO and J. M. HONING, *Trans. Faraday Soc.* **54**(7) (1958) 1067.
51. J. F. MAMMONE, S. K. SHARMA and M. NICOL, *Solid State Commun.* **34** (1980) 799.
52. J. L. MURRAY and H. A. WRIEDT, *Bull. Alloy Phase Diag.* **8**(2) (1987) 148.
53. A. W. WEEBER and H. BAKKER, *Physica B* **153** (1988) 93.
54. R. B. SCHWARZ and C. C. KOCH, *Appl. Phys. Lett.* **49**(3) (1986) 146.
55. U. MIZUTANI and C. H. LEE, *J. Mater. Sci.* **25** (1990) 399.
56. C. C. KOCH, *React. Solids* **8** (1989) 283.
57. D. R. MAURICE and T. H. COURTNEY, *Metall. Trans.* **21A** (1990) 289.
58. G. B. SCHAFFER and P. G. MCCORMICK, *ibid.* **23A** (1992) 1285.
59. R. M. DAVIS, B. MCDERMOTT, and C. C. KOCH, *ibid.* **19A** (1988) 2867.
60. A. W. CZANDERNA, C. N. R. RAO and J. M. HONING, *Trans. Faraday Soc.* **54**(7) (1958) 1067.
61. J. ECKERT, L. SCHULTZ, E. HELLSTERN and K. URBAN, *J. Appl. Phys.* **64**(6) (1988) 3224.
62. Z.-G. YANG, R.-M. REN and L. SHAW, *J. Am. Ceram. Soc.* submitted.
63. H. HERMANN, TH. SCHUBERT, W. GRUNER and N. MATTERN, *Nanostruct. Mater.* **8**(2) (1997) 215.
64. I. BARIN and O. KNACKE, "Thermochemical Properties of Inorganic Substances" (Spinger-Verlag, Berlin, Germany, 1973).
65. M. MIYAYAMA and H. YANAGIDA, in "Engineering Materials Handbook, Vol. 4: Ceramics and Glasses," edited by S. J. Schneider (ASM International, Materials Park, OH, 1991).

Received 10 February 1999
and accepted 26 April 2000